

Semi-Supervised Hyperspectral Image Classification with Edge-Aware Superpixel Label Propagation and Adaptive Pseudo-Labeling

Yunfei Qiu, Qiqiong Ma, Tianhua Lv, Li Fang, *Senior Member, IEEE*,
Shudong Zhou, and Wei Yao, *Senior Member, IEEE*

Abstract—Significant progress has been made in semi-supervised hyperspectral image (HSI) classification regarding feature extraction and classification performance. However, due to high annotation costs and limited sample availability, semi-supervised learning still faces challenges such as boundary label diffusion and pseudo-label instability. To address these issues, this paper proposes a novel semi-supervised hyperspectral classification framework integrating spatial prior information with a dynamic learning mechanism. First, we design an Edge-Aware Superpixel Label Propagation (EASLP) module. By integrating edge intensity penalty with neighborhood correction strategy, it mitigates label diffusion from superpixel segmentation while enhancing classification robustness in boundary regions. Second, we introduce a Dynamic History-Fused Prediction (DHP) method. By maintaining historical predictions and dynamically weighting them with current results, DHP smoothens pseudo-label fluctuations and improves temporal consistency and noise resistance. Concurrently, incorporating confidence and consistency measures, the Adaptive Tripartite Sample Categorization (ATSC) strategy implements hierarchical utilization of easy, ambiguous, and hard samples, leading to enhanced pseudo-label quality and learning efficiency. The Dynamic Reliability-Enhanced Pseudo-Label Framework (DREPL), composed of DHP and ATSC, strengthens pseudo-label stability across temporal and sample domains. Through synergizes operation with EASLP, it achieves spatio-temporal consistency optimization. Evaluations on four benchmark datasets demonstrate its capability to maintain superior classification performance.

Index Terms—Hyperspectral image classification, semi-supervised learning, superpixel label propagation, dynamic pseudo-labeling

I. INTRODUCTION

HYPERSPECTRAL image (HSI) provides more continuous and detailed spectral band information, enabling it to capture subtle spectral differences in terrestrial materials. As a crucial application, hyperspectral image classification (HSIC) can assign precise land cover labels to each observed pixel, and thus has gained increasing attention [1]–[6]. However, it is confronted with two major challenges: on one hand, the complex high-dimensional structure of HSI complicates feature extraction, which can be addressed through deep learning techniques [7]; on the other hand, the labor-intensive and time-consuming nature of manual annotation makes it difficult to obtain large labeled datasets [8]–[10], presenting a

Y. Qiu, Q. Ma, and T. Lv are with Liaoning Technical University, Huludao, Liaoning, China.

Q. Ma and T. Lv are also with the State Key Laboratory of Regional and Urban Ecology, Institute of Urban Environment, Chinese Academy of Sciences, Xiamen, China.

L. Fang (corresponding author), S. Zhou, and W. Yao are with the State Key Laboratory of Regional and Urban Ecology, Institute of Urban Environment, Chinese Academy of Sciences, Xiamen, China (e-mail: lfang@iue.ac.cn).

significant challenge for deep learning models that typically require substantial training data, thereby driving the need for techniques that enhance classification performance under constrained supervision.

The early stages of HSIC research witnessed considerable advances with the adoption of fully supervised methods based on convolutional neural networks (CNNs) [11]–[14], e.g., Contextual Deep CNN [15], SSRN [16], and HybridSN [17]. As representative models, A2S2K [18] and SSTN [19] further strengthened feature representation capabilities through adaptive convolutional kernels and spectral–spatial transformation structures [20]. Nevertheless, these methods remain fundamentally constrained by their heavy reliance on large-scale high-quality annotations, making them impractical for hyperspectral scenarios with prohibitive labeling costs.

Addressing this challenge, increasing attention has turned to unsupervised learning [21]. Autoencoders (AEs) and their variants have been extensively employed for HSI feature learning, e.g., Denoising Autoencoder (DAE) [22], Stacked Sparse Autoencoder (SSAE) [23], spectral–spatial partitional clustering techniques [24], Superpixel-based Unsupervised Linear Discriminant Analysis model (S3-ULDA) [25], and related unsupervised methodologies. Despite the advantages in feature compression, denoising, and spectral–spatial fusion, these approaches struggle to capture complex inter-class relationships, resulting in limited classification performance.

In recent years, growing research efforts have been directed toward self-supervised pretraining to alleviate feature learning challenge in few-shot scenarios [26]–[28], [31]. For instance, DEMA [29] leveraged both feature reconstruction and contrastive constraints for feature initialization under unlabeled conditions, while RMAE [30] further integrated limited labeled data for joint optimization, demonstrating feature transfer potential in few-shot settings. However, their focus on feature pretraining often neglects pseudo-label stability and decision boundary robustness, limiting performance in complex scenarios.

In this context, semi-supervised learning has progressively emerged as a focal point for HSIC research [32]–[35]. It combines limited labeled data with abundant unlabeled data, simultaneously leveraging label information from supervised learning and self-learning capabilities from unsupervised methodologies [36]. The graph-based semi-supervised learning framework was first proposed by Zhu et al. [37], where both labeled and unlabeled data are represented as vertices in a weighted graph and classification is achieved using harmonic functions. A significant advancement emerged with consistency regularization methods [38], [39], exemplified by the Mean Teacher

model [40] that improves unlabeled data utilization through consistency regularization. Advancing this line of work, [41] devised a graph-structured semi-supervised generative model that substantially improves pseudo-label stability through dual-branch consistency constraints. Concurrently, [42] further integrated convolutional and Transformer architectures while introducing cross-modal consistency regularization, thereby capturing spectral–spatial long-range dependencies and simultaneously boosting model generalization. Collectively, existing methods have improved pseudo-label utilization efficiency to some extent. However, they still fall short in label propagation within boundary regions and suppression of pseudo-label noise, which presents significant opportunities for future research [43], [44].

Grounded in the preceding analysis, this paper proposes an innovative semi-supervised framework integrating spatial prior with dynamic learning for HSI classification. This comprehensive solution targets critical limitations in boundary label diffusion, pseudo-label instability [45], and sample uncertainty [46], [47], systematically enhancing training reliability with scarce labels. Its efficacy has been extensively validated across multiple benchmark datasets.

In summary, the key contributions of our work are stated as follows.

1) **Edge-Aware Superpixel Label Propagation(EASLP):**

Through the synergistic combination of edge intensity penalty mechanism and neighborhood correction strategy, the approach effectively addresses label diffusion at boundaries in superpixel-based propagation.

2) **Dynamic History-Fused Prediction (DHP):** By preserving historical predictions and performing dynamic weighting with current outputs, the approach stabilizes pseudo-label generation, effectively mitigating training fluctuations.

3) **Adaptive Tripartite Sample Categorization (ATSC):**

The framework adaptively classifies unlabeled samples into easy, ambiguous, and hard types according to confidence–consistency measures. It strategically assigns differentiated loss weights through dynamic thresholds based on categorical learning difficulty.

4) **Dynamic Reliability-Enhanced Pseudo-Labeling (DREPL):** Unifying DHP and ATSC, DREPL enhances pseudo-label quality through temporal consistency and sample reliability.

This paper begins with a detailed presentation of the proposed framework in Section II. Section III continues with a comprehensive analysis of the experimental results obtained from several public datasets. The paper ends with conclusions and future research direction in Section IV.

II. METHODOLOGY

The overall workflow of the proposed semi-supervised HSIC method is illustrated in Fig 1.

For labeled data, weak augmentation Aug_w is first applied before being fed into a shared feature extraction network. The processed features then pass through a classification head, and the predictions are computed with the ground truth labels to calculate the supervised loss \mathcal{L}_{sup} .

Unlabeled data first acquires spatial constraints via EASLP to address label diffusion along boundaries, then follows a dual-path augmentation scheme (Aug_w/Aug_s) feeding into shared feature extraction. The weak augmentation Aug_w path flows into DHP and ATSC-based pseudo-label generation, while the strong augmentation Aug_s path computes the unsupervised loss $\mathcal{L}_{\text{unsup}}$ under pseudo-label guidance. This integrated DHP-ATSC framework establishes the proposed DREPL framework.

A. Edge-Aware Superpixel Label Propagation (EASLP)

To address label propagation issues at the boundaries, the EASLP module incorporates an edge intensity penalty mechanism during the composition stage, adaptively suppressing label diffusion across the boundaries. Following propagation, an edge-sensitive neighborhood correction strategy is employed to further refine the labels of boundary pixels. This module can be seamlessly integrated with the backbone framework for structural enhancement in pseudo-label generation.

The process begins by applying the Simple Linear Iterative Clustering (SLIC) algorithm [48] to perform superpixel segmentation on the input HSI, yielding several non-overlapping regions with strong spatial–spectral consistency (as shown in Fig 1). These regions are divided into multiple superpixel clusters (e.g., S_1, S_2, S_3, S_4, S_5 , etc.). It contains labeled data (e.g., categories C_1, C_2, C_3) as well as unlabeled data (e.g. U_1, U_2, U_3). Based on whether each superpixel contains labeled samples, they are categorized into two types: superpixels containing labeled samples (e.g., S_2, S_4) and superpixels without labeled samples (e.g., S_1, S_3, S_5).

For superpixels containing labeled samples, we count the number of samples per category and propagate the most frequent category label to all unlabeled samples within that superpixel.

For superpixels without labeled samples, the cosine similarity between their spectral mean and the spectral mean of each training sample category is computed, serving as a matching score for label prediction.

$$\text{Sim}_{ij} = \frac{\mathbf{v}_i \cdot \mathbf{v}_j}{\|\mathbf{v}_i\| \cdot \|\mathbf{v}_j\|} \quad (1)$$

where \mathbf{v}_i denotes the spectral mean of the training samples in the i -th class; \mathbf{v}_j denotes the spectral mean of the unlabeled superpixels j .

To prevent the propagation of erroneous labels in boundary regions, we introduce an edge intensity map based on the Sobel filter to explicitly incorporate spatial structural constraints during similarity propagation. Specifically, the Sobel operator is a first-order gradient operator that calculates the rate of grayscale variation in both horizontal and vertical directions within an image, thereby detecting edge structures of features or objects.

Firstly, we take the mean along the spectral dimension of the hyperspectral data $\mathbf{X} \in \mathbb{R}^{H \times W \times B}$ to obtain a 2-D grayscale image I .

$$I(x, y) = \frac{1}{B} \sum_{b=1}^B \mathbf{X}(x, y, b) \quad (2)$$

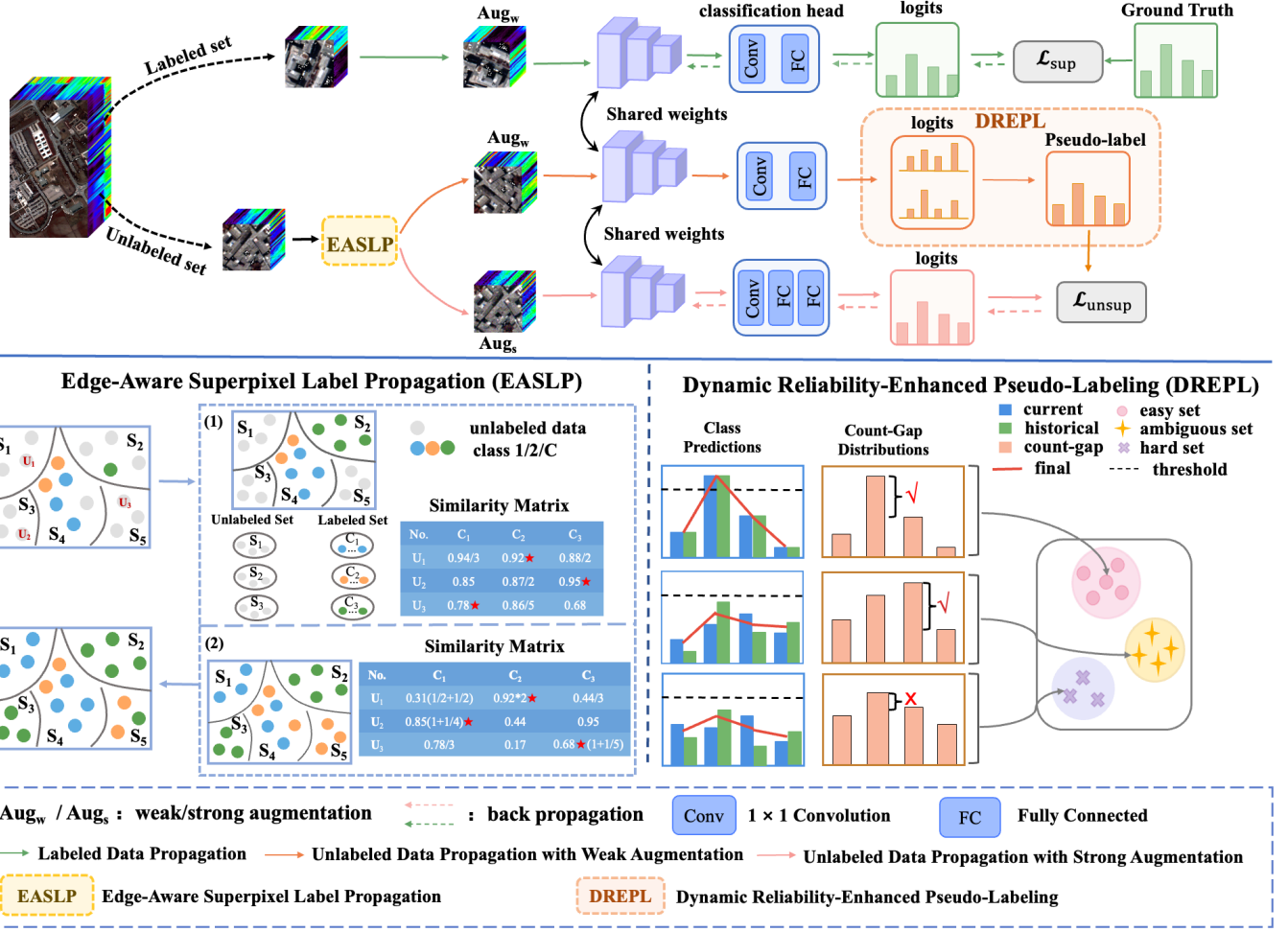


Fig. 1. The overall framework of the proposed semi-supervised HSIC method.

Subsequently, a Sobel filter is applied to I to compute the gradient magnitude for each pixel.

$$E(x, y) = \sqrt{(G_x * I)^2 + (G_y * I)^2} \quad (3)$$

where G_x and G_y represent Sobel's fixed convolution kernels in the horizontal and vertical directions, respectively.

$$G_x = \begin{bmatrix} -1 & 0 & +1 \\ -2 & 0 & +2 \\ -1 & 0 & +1 \end{bmatrix}, \quad G_y = \begin{bmatrix} -1 & -2 & -1 \\ 0 & 0 & 0 \\ +1 & +2 & +1 \end{bmatrix}. \quad (4)$$

The resulting $E(x, y)$ reflects the local intensity of grayscale variation at each pixel, i.e., the edge significance. This edge intensity map is normalized and used to evaluate the average edge response for each superpixel region.

$$E_j = \frac{1}{|S_j|} \sum_{(x, y) \in S_j} E(x, y), \quad (5)$$

where E_j denotes the average edge intensity of the j -th superpixel; $|S_j|$ represents the number of pixels within the superpixel region S_j .

During the similarity propagation stage, the edge intensity serves as a penalty factor to dynamically weight the similarity scores derived from cosine similarity. The weight is calculated as follows.

$$\tilde{\text{Sim}}_{ij} = \frac{\text{Sim}_{ij}}{1 + E_j} \quad (6)$$

Compared to weight functions in logarithmic or exponential forms, this linear decay strategy maintains higher similarity scores when $E_j \rightarrow 0$, while automatically attenuating the propagation effect when E_j becomes large. This mechanism achieves a more robust balance between edge and non-edge regions. The first similarity matrix is obtained by computing the cosine similarity and weighting it with the edge intensity derived from the Sobel filter.

Based on this matrix, the unlabeled regions U_1 , U_2 , and U_3 are assigned to categories C_2 , C_3 , and C_1 , respectively, as illustrated in Fig 1.

Furthermore, to enhance the stability of pseudo-labels in boundary region, we design a neighborhood-based edge-weighted correction mechanism. Specifically, each unlabeled superpixel collects label votes from its adjacent superpixels, with weights assigned according to the edge intensity of its

neighbors. In this way, the label \hat{y}_j for each superpixel j is obtained. The correction formula is defined as follows.

$$\hat{y}_j = \arg \max_c \sum_{k \in \mathcal{N}(j)} \frac{1}{E_k + \epsilon} \cdot \mathbb{I}[y_k = c] \quad (7)$$

where $\mathcal{N}(j)$ denotes the neighborhood set of superpixel j , E_k represents the edge intensity of adjacent superpixel k , $\mathbb{I}[y_k = c]$ is the indicator function that equals 1 when the label of k is c and 0 otherwise, and $\epsilon = 10^{-6}$ is a small constant to prevent division by zero.

Therefore, regions with weaker edges exert greater influence on label propagation, thereby guiding pseudo-labels toward areas of strong internal consistency and preventing their propagation across category boundaries. Finally, the second similarity matrix is obtained by computing the neighbor-voting mechanism followed by edge-aware processing. Based on this refined matrix, the label of U_2 is revised from category C_3 to category C_1 .

Upon completion of the entire process, we generate a structure-aware pseudo-label map and perform balanced sampling of unlabeled training samples from each pseudo-label category to support semi-supervised training.

B. Dynamic History-Fused Prediction (DHP)

To address the issue of temporal fluctuation in pseudo labels, we propose a DHP method that leverages historical information to improve the pseudo-label stability, with its overall structure illustrated in Fig 1.

1) *Historical Prediction Queue Modeling*: Initially, a historical prediction queue is maintained for each unlabeled sample, recording its categorical prediction frequencies over the most recent T iterations.

Specifically, the historical prediction queue is given by:

$$Q_i^{(t)} = \{\text{cnt}_i^{(t)}(C_1), \text{cnt}_i^{(t)}(C_2), \dots, \text{cnt}_i^{(t)}(C_K)\} \quad (8)$$

where $Q_i^{(t)}$ denotes the historical prediction statistics of sample u_i at the t -th training epoch, $\text{cnt}_i^{(t)}(C_k)$ ($k = 1, \dots, K$) represents the frequency with which sample u_i is predicted as category C_k over the most recent T iterations.

2) *Queue Update and Growth Strategy*: Subsequently, an exponential growth strategy is employed to dynamically adjust the historical prediction queue length L .

The queue length update rule is defined as:

$$L(t) = L_{\min} \cdot \left(\frac{L_{\max}}{L_{\min}} \right)^{\frac{t}{T_{\max\text{Epoch}}}} \quad (9)$$

where L_{\min} and L_{\max} represent the minimum and maximum queue length, respectively, t denotes the current training epoch, and $T_{\max\text{Epoch}}$ indicates the total number of training epochs.

3) *Dynamic Weighted Fusion Strategy*: We introduce a dynamic weighted fusion strategy to effective integration of historical and current predictions. Defining P_{cur} and P_{hist} as the current and historical prediction distributions, respectively, the final fused distribution is formulated as:

$$P_{\text{fuse}}(u_i) = (1 - \alpha)P_{\text{cur}}(u_i) + \alpha P_{\text{hist}}(u_i), \quad (10)$$

$$P_{\text{hist}}(u_i) = \frac{\text{cnt}_i^{(t)}(k)}{\sum_{k=1}^K \text{cnt}_i^{(t)}(k)} \quad (11)$$

where α represents the weight assigned to historical predictions, being gradually incremented throughout training, with its evolution governed by:

$$\alpha_t = \min \left(\alpha_{\min}, \alpha_{\min} + (\alpha_{\max} - \alpha_{\min}) \cdot \frac{t - t_0}{T_{\max\text{Epoch}} - t_0} \right) \quad (12)$$

where α_{\min} and α_{\max} denote the minimum and maximum weight values, respectively, t_0 represents the epoch at which historical predictions are first incorporated. As illustrated in Fig 1, the category prediction is obtained through a weighted fusion of historical and current predictions, thereby effectively smoothing the prediction distribution and yielding more stable and reliable pseudo-labels.

C. Adaptive Tripartite Sample Categorization(ATSC)

1) *Confidence-Driven Sample Selection*: For quantitative assessment of prediction stability, the Count-Gap (CG) metric is introduced, utilizing temporally accumulated prediction records from unlabeled sample. The metric calculates the frequency disparity between the top-two most frequently predicted categories:

$$CG(u_i) = f_{\max}(u_i) - f_{\text{second}}(u_i) \quad (13)$$

where $f_{\max}(u_i)$ denotes the count of times the sample u_i is predicted as the most frequent category, and $f_{\text{second}}(u_i)$ represents the corresponding count for the second most frequent category.

2) *Adaptive Sample Classification*: Utilizing the historical consistency measure, the framework employs the fused prediction distribution $P_{\text{fuse}}(u_i)$ for adaptive classification of unlabeled samples. The procedure commences with calculating the prediction confidence per sample:

$$\text{Conf}(u_i) = \max(P_{\text{fuse}}(u_i)) \quad (14)$$

Based on the confidence and CG values, we adopt a dual-threshold strategy, as illustrated in Fig 1, to categorize unlabeled samples into three distinct classes:

Easy samples: Confidence score $\text{Conf}(u_i) \geq \tau_a$ and $CG \geq \tau_e$. The pseudo-labels are reliable and can be directly incorporated into training.

Ambiguous samples: Confidence score $\text{Conf}(u_i) < \tau_a$ and $CG > \tau_e$, indicating unstable predictions that require cautious utilization.

Hard samples: Confidence score $\text{Conf}(u_i) < \tau_a$ and $CG < \tau_e$, indicating significant prediction fluctuations. Such samples are temporarily discarded to avoid introducing noise.

3) *Adaptive Threshold Update Mechanism*: To further enhance the flexibility of sample categorization, we dynamically update thresholds τ_a and τ_c using an exponential moving average (EMA) mechanism.

$$\tau_a^{(t)} = m \cdot \tau_a^{(t-1)} + (1-m) \cdot \mu_a^{(t)}, \quad \mu_a^{(t)} = \frac{1}{B_u} \sum_{i=1}^{B_u} CG_i \quad (15)$$

$$\tau_c^{(t)} = m \cdot \tau_c^{(t-1)} + (1-m) \cdot \mu_c^{(t)}, \quad \mu_c^{(t)} = \frac{1}{B_u} \sum_{i=1}^{B_u} \max(P_{\text{fuse}}(u_i)) \quad (16)$$

where m indicates the smoothing coefficient and $\tau^{(t)}$ denotes the candidate threshold computed for the current batch B_u .

This adaptive partitioning method overcomes the limitations of binary approaches and enhances the utilization efficiency of pseudo labels.

D. Loss Function

1) *Supervised Loss*: The labeled data objective minimizes the standard cross-entropy loss:

$$\mathcal{L}_{\text{sup}} = -\frac{1}{N_l} \sum_{i=1}^{N_l} \log p(y_i | x_i) \quad (17)$$

where N_l denotes the number of labeled samples, x_i denotes the input data of the i -th labeled sample, y_i represents the true label, and $p(\cdot)$ is the predicted probability distribution.

2) *Self-training Loss for Unlabeled Samples*: A differentiated loss scheme is implemented for unlabeled samples according to pseudo-label confidence and CG metric, following a tripartite division into easy, ambiguous, and hard categories.

Easy samples: High confidence and strong consistency indicate reliable pseudo-labels, permitting the direct application of cross-entropy loss.

$$\mathcal{L}_{\text{easy}} = -\frac{1}{N_e} \sum_{i \in \mathcal{E}} \log p(\hat{y}_i | u_i^{\text{strong}}) \quad (18)$$

where \hat{y}_i indicates the generated pseudo-label and u_i^{strong} denotes strongly augmented samples.

Ambiguous samples: Samples characterized by intermediate or fluctuating confidence levels are supervised using temperature-scaled soft prediction distribution $p(\cdot)$ rather than hard pseudo-labels. The consistency is regularized through KL divergence as follows.

$$\mathcal{L}_{\text{amb}} = \frac{1}{N_a} \sum_{i \in \mathcal{A}} D_{\text{KL}}(\tilde{p}(u_i^{\text{weak}}) \| p(u_i^{\text{strong}})) \quad (19)$$

where \mathcal{A} is the ambiguous sample set, while $\tilde{p}(u_i^{\text{weak}})$ and $p(u_i^{\text{strong}})$ correspond to the soft prediction distributions under weak and strong augmentation, respectively.

Hard samples: Samples with excessively low confidence and significant prediction fluctuations are directly discarded to avoid the detrimental effects of misleading noisy labels.

The overall self-training loss for unlabeled samples is formulated below.

$$\mathcal{L}_{\text{unsup}} = \mathcal{L}_{\text{easy}} + \lambda_a \cdot \mathcal{L}_{\text{amb}} \quad (20)$$

where λ_a is a dynamically adjusted weight during training that controls the contribution of ambiguous samples.

3) *Overall Objective*: In summary, the model's final optimization objective is expressed by:

$$\mathcal{L} = \mathcal{L}_{\text{sup}} + \mathcal{L}_{\text{unsup}}, \quad (21)$$

Specifically, it jointly optimizes the supervised classification loss on labeled samples and the self-training loss on unlabeled samples.

III. EXPERIMENTS AND ANALYSIS

A. Dataset Details

A comprehensive evaluation of the proposed method is conducted employing four benchmark HSI datasets: Pavia University (PaviaU), Houston2013, Kennedy Space Center (KSC), and Botswana. Spanning urban, forests, wetlands, and agricultural scenarios with distinct spectral-spatial features, these datasets enable rigorous evaluation of methodological robustness and generalization in complex settings. Detailed parameters (image size, spectral bands, and per-class labeled samples) for all datasets are summarized in Table I.

B. Experimental Setup

The implementation is built upon the PyTorch framework, with all experiments trained on an NVIDIA RTX 2080 Ti GPU for computational efficiency. A standardized preprocessing pipeline is applied to the input HSI data: linear normalization of reflectance values to [0,1], followed by division into 24×24 pixel patches that are converted into three-dimensional cubes compatible with the network architecture.

The study adopts balanced class sampling, randomly selecting 10 samples per class for training while reserving the remainder for testing. To ensure robust statistical analysis, all experiments are repeated through 10 independent trials with averaged results reported. The Adam optimizer is configured with an initial learning rate of 1×10^{-3} for 200 training epochs. Performance evaluation comprehensively measures Overall Accuracy (OA), Average Accuracy (AA), and the Kappa coefficient.

A dual-path data augmentation scheme addresses overfitting and boosts generalization: weak augmentation utilizes random flipping for sample diversification, while strong augmentation incorporates random noise disturbances to mimic imaging artifacts in complex environments.

The quantity of superpixels M in the segmentation module is a function of the image size parameters ($H \times W$) and the target pixel count per superpixel ϵ , which is computed by:

$$M = \frac{H \times W}{\epsilon} \quad (22)$$

where ϵ denotes the pixel count per superpixel. For parameter configuration, Houston2013 uses $\epsilon = 200$ while a standard value of $\epsilon = 50$ is applied to the remaining datasets.

TABLE I
DETAILED PARAMETER INFORMATION FOR DIFFERENT DATASETS.

Dataset	PaviaU			Houston2013			KSC			Botswana		
Sensor	ROSIS			CASI-1500			AVIRIS			Hyperion		
Size & Bands	610 × 340 × 103			349 × 1905 × 144			512 × 614 × 176			1476 × 256 × 145		
Class	Name	Test	Training	Name	Test	Training	Name	Test	Training	Name	Test	Training
1	Asphalt	10	6621	Healthy Grass	10	1241	Scrub	10	751	Water	10	260
2	Meadows	10	18639	Stressed Grass	10	1244	Willow Swamp	10	233	Hippo Grass	10	91
3	Gravel	10	2089	Synthetic Grass	10	687	Cabbage Palm Hammock	10	246	Floodplain Grasses 1	10	241
4	Trees	10	3054	Trees	10	1234	Cabbage Palm/Oak	10	242	Floodplain Grasses 2	10	205
5	Painted Metal Sheets	10	1335	Soil	10	1232	Slash Pine	10	151	Reeds	10	259
6	Bare Soil	10	5019	Water	10	315	Oak/Broadleaf	10	219	Riparian	10	259
7	Bitumen	10	1320	Residential	10	1258	Hardwood Swamp	10	95	Firescar	10	249
8	Self-blocking Bricks	10	3672	Commercial	10	1234	Graminoid Marsh	10	421	Island Interior	10	193
9	Shadows	10	937	Road	10	1242	Spartina Marsh	10	510	Acacia Woodlands	10	304
10	—	—	—	Highway	10	1217	Cattail Marsh	10	394	Acacia Shrublands	10	238
11	—	—	—	Railway	10	1225	Salt Marsh	10	409	Acacia Grasslands	10	295
12	—	—	—	Parking Lot 1	10	1223	Mud Flats	10	493	Short Mopane	10	171
13	—	—	—	Parking Lot 2	10	459	Water	10	917	Mixed Mopane	10	258
14	—	—	—	Tennis Court	10	418	—	—	—	Exposed Soils	10	85
15	—	—	—	Running Track	10	650	—	—	—	—	—	—
Total		90	42686		150	14879		130	5081		140	3108

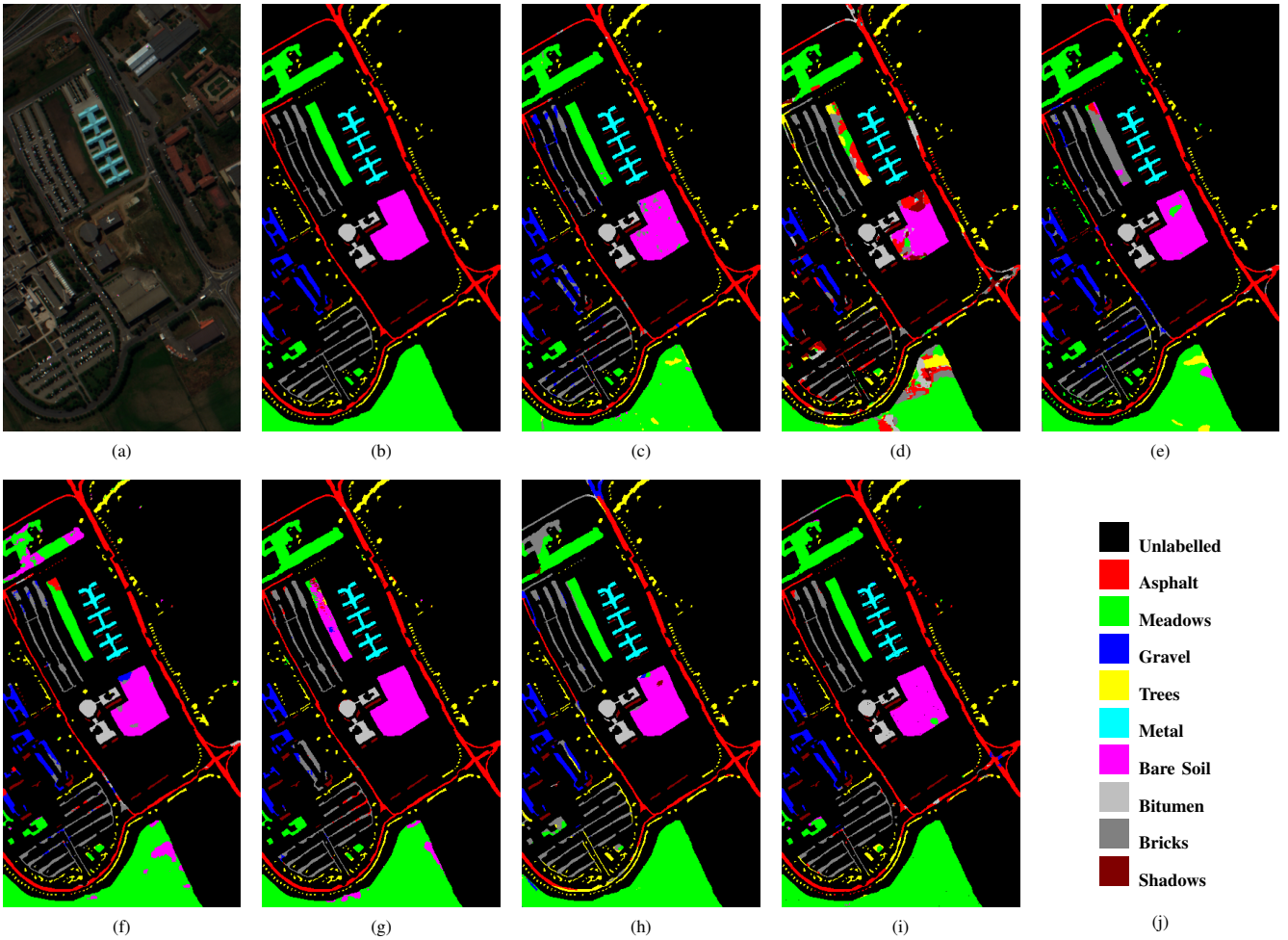


Fig. 2. Classification maps for the PaviaU dataset. (a) False color image. (b) Ground-truth. (c) A2S2K. (d) DMSGer. (e) SSTN. (f) CTF-SSCL. (g) DEMAЕ. (h) RMAE. (i) Ours. (j) Color labels.

C. Performance Comparison

Comparative analyses include two fully-supervised baselines (A2S2K [18], SSTN [19]), two semi-supervised models (DMSGer [41], CTF-SSCL [42]), and two few-shot self-

supervised methods (DEMAЕ [29], RMAE [30]). Tables II–V summarize the classification accuracy of various methods, with the corresponding classification maps illustrated in Fig. 2–5.

On the PaviaU dataset, the proposed method exhibits su-

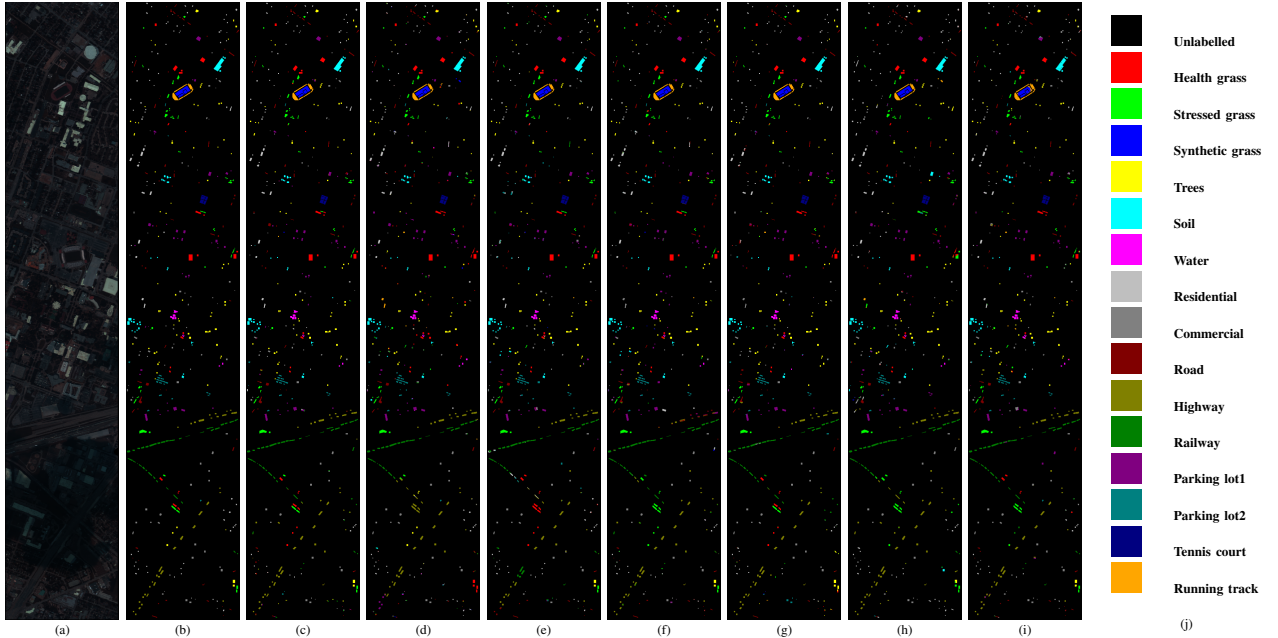


Fig. 3. Classification maps for the Houston2013 dataset. (a) False color image. (b) Ground-truth. (c) A2S2K. (d) DMSGer. (e) SSTN. (f) CTF-SSCL. (g) DEMAЕ. (h) RMAЕ. (i) Ours. (j) Color labels

TABLE II
CLASSIFICATION RESULTS FOR THE PAVIAU DATASET WITH 10 LABELED SAMPLES PER CLASS.

No.	A2S2K	DMSGer	SSTN	CTF-SSCL	DEMAЕ	RMAЕ	Ours
1	73.06 ± 6.43	69.71 ± 4.60	91.83 ± 1.26	91.95 ± 3.64	87.03 ± 5.36	79.18 ± 1.61	88.28 ± 5.45
2	88.29 ± 4.58	87.27 ± 5.47	79.59 ± 3.44	80.52 ± 8.72	90.98 ± 8.75	93.76 ± 2.22	97.47 ± 1.59
3	81.58 ± 2.14	91.46 ± 7.06	91.87 ± 4.35	84.32 ± 4.86	83.32 ± 9.11	90.37 ± 4.41	94.04 ± 1.36
4	96.80 ± 0.97	84.92 ± 5.49	79.13 ± 4.80	92.69 ± 3.42	94.55 ± 2.57	98.72 ± 0.49	91.63 ± 4.43
5	100.00 ± 0.00	99.80 ± 0.19	99.98 ± 0.03	99.81 ± 0.24	99.75 ± 0.29	99.42 ± 0.15	98.15 ± 2.40
6	91.27 ± 4.39	95.75 ± 1.55	97.36 ± 2.97	88.29 ± 8.39	95.33 ± 4.97	99.94 ± 0.06	97.66 ± 2.77
7	98.98 ± 1.11	98.88 ± 3.44	98.14 ± 4.04	97.66 ± 1.90	99.20 ± 0.72	99.97 ± 0.06	98.36 ± 2.86
8	60.79 ± 6.03	92.47 ± 3.59	83.91 ± 4.76	88.42 ± 6.91	85.53 ± 5.74	92.48 ± 0.79	95.57 ± 3.07
9	99.59 ± 0.32	98.85 ± 0.52	99.53 ± 0.40	98.32 ± 1.18	98.09 ± 1.14	94.13 ± 0.65	91.47 ± 7.74
OA (%)	86.94 ± 1.32	87.00 ± 2.62	86.15 ± 1.26	86.47 ± 4.24	90.98 ± 3.87	92.68 ± 0.73	95.21 ± 1.17
AA (%)	87.26 ± 1.28	90.90 ± 1.43	91.26 ± 0.92	91.33 ± 1.94	92.64 ± 1.53	94.22 ± 0.32	94.46 ± 1.48
$\kappa \times 100$	85.30 ± 1.48	83.30 ± 1.17	82.27 ± 1.54	82.74 ± 5.11	88.32 ± 4.78	90.46 ± 0.90	93.67 ± 1.54

perior performance, as shown in Table II, attaining 95.21% OA, 94.46% AA, and 93.67% Kappa—surpassing RMAE by 2.53%, 0.24%, and 3.21%, respectively. In terms of per-class accuracy, the proposed model performs better across most land-cover categories, particularly in Meadows, Gravel, and Self-blocking bricks (Classes 2, 3, and 8). As illustrated in Fig 2, the classification map produced by the proposed method exhibits smoother boundary transitions and more complete regional delineation.

The proposed method achieves notable results on the Houston 2013 dataset (Table III), with OA/AA/Kappa values of 89.77%/90.87%/88.94%, representing significant enhancement of 1.75%/1.94%/2.77% over DEMAЕ. It exhibits clear superiority in classifying buildings, grass, and low vegetation categories. The visually evident boundary blurring in DEMAЕ’s outputs underscores our method’s enhanced boundary

definition capacity (Fig 3).

As shown in Table IV, the proposed method achieves remarkable performance on the KSC dataset, with OA, AA, and Kappa rechieving 99.71%, 99.48%, and 99.68%, respectively—exceeding DEMAЕ by 0.49%, 0.38%, and 0.55%. The model demonstrates near-perfect accuracy for vegetation, soil, and wetland categories, indicating strong discriminative power and generalization capability.

For the Botswana dataset (Table V), the proposed method achieves 99.19% OA, 99.22% AA, and 99.12% Kappa, outperforming RMAE by 0.36%, 0.19%, and 0.39%. Although SSTN attains near-saturated overall accuracy, its limited capacity for capturing local details results in marginally reduced comprehensive performance. Other competing methods, heavily reliant on massive labeled samples, perform relatively inferior performance under limited annotation conditions. These

TABLE III
CLASSIFICATION RESULTS FOR THE HOUSTON2013 DATASET WITH 10 LABELED SAMPLES PER CLASS.

No.	A2S2K	DMSGer	SSTN	CTF-SSCL	DEMAE	RMAE	Ours
1	84.69 \pm 1.14	85.37 \pm 8.00	97.13 \pm 2.71	93.17 \pm 5.76	90.09 \pm 13.03	76.51 \pm 5.24	86.67 \pm 6.13
2	97.99 \pm 1.09	78.91 \pm 4.96	91.77 \pm 5.21	89.55 \pm 7.96	87.52 \pm 7.22	80.55 \pm 3.69	88.64 \pm 4.60
3	99.94 \pm 0.07	97.51 \pm 0.77	99.46 \pm 1.03	98.92 \pm 1.33	99.23 \pm 0.58	99.91 \pm 0.12	95.79 \pm 4.52
4	92.88 \pm 0.94	66.65 \pm 6.03	94.02 \pm 2.55	95.44 \pm 2.93	92.01 \pm 5.53	74.02 \pm 2.57	87.60 \pm 5.00
5	100.00 \pm 0.00	99.86 \pm 0.22	99.15 \pm 0.73	98.69 \pm 1.47	99.89 \pm 0.25	99.55 \pm 0.92	99.33 \pm 0.83
6	98.95 \pm 0.94	99.91 \pm 0.29	83.93 \pm 2.94	90.79 \pm 6.17	94.83 \pm 5.75	92.16 \pm 3.16	89.91 \pm 5.74
7	78.86 \pm 3.62	71.87 \pm 3.41	77.49 \pm 5.55	79.17 \pm 6.23	80.14 \pm 11.03	85.37 \pm 1.06	87.84 \pm 3.26
8	56.13 \pm 2.64	51.26 \pm 4.51	53.64 \pm 6.40	62.75 \pm 7.70	67.06 \pm 7.95	67.58 \pm 5.25	69.55 \pm 8.87
9	76.89 \pm 4.16	70.79 \pm 5.16	84.75 \pm 4.00	77.79 \pm 6.68	78.86 \pm 5.75	59.51 \pm 3.73	88.80 \pm 3.56
10	77.18 \pm 5.01	89.31 \pm 4.42	86.45 \pm 8.24	88.05 \pm 10.09	93.45 \pm 9.22	99.52 \pm 0.61	98.54 \pm 1.53
11	84.57 \pm 5.41	75.14 \pm 6.20	87.68 \pm 6.28	79.97 \pm 12.42	85.82 \pm 14.58	86.16 \pm 2.07	90.73 \pm 7.21
12	75.65 \pm 5.88	86.23 \pm 3.45	51.14 \pm 10.19	83.18 \pm 10.32	77.45 \pm 8.00	80.10 \pm 4.82	87.46 \pm 4.24
13	91.85 \pm 0.75	89.85 \pm 2.57	82.57 \pm 6.82	92.92 \pm 4.47	87.63 \pm 7.22	73.83 \pm 3.85	95.95 \pm 2.27
14	100.00 \pm 0.00	100.00 \pm 0.00	99.77 \pm 0.46	99.45 \pm 0.89	100.00 \pm 0.00	99.67 \pm 0.62	99.04 \pm 1.98
15	100.00 \pm 0.00	100.00 \pm 0.00	100.00 \pm 0.00	99.57 \pm 0.82	100.00 \pm 0.00	99.71 \pm 0.55	98.28 \pm 2.48
OA (%)	85.21 \pm 0.97	80.93 \pm 1.24	84.41 \pm 0.84	86.86 \pm 1.79	87.20 \pm 2.41	83.10 \pm 0.64	89.77 \pm 1.17
AA (%)	87.71 \pm 0.77	84.20 \pm 1.03	85.93 \pm 0.82	88.63 \pm 1.66	88.93 \pm 2.26	84.94 \pm 0.43	90.87 \pm 0.98
$\kappa \times 100$	84.02 \pm 1.05	79.40 \pm 1.34	83.15 \pm 0.90	85.80 \pm 1.93	86.17 \pm 2.60	81.73 \pm 0.69	88.94 \pm 1.26

TABLE IV
CLASSIFICATION RESULTS FOR THE KSC DATASET WITH 10 LABELED SAMPLES PER CLASS.

No.	A2S2K	DMSGer	SSTN	CTF-SSCL	DEMAE	RMAE	Ours
1	97.64 \pm 2.06	93.59 \pm 6.36	99.41 \pm 0.54	98.12 \pm 1.01	99.61 \pm 0.80	89.32 \pm 5.00	99.84 \pm 0.19
2	98.88 \pm 0.95	78.45 \pm 0.26	81.13 \pm 6.46	97.08 \pm 1.88	99.87 \pm 0.27	96.61 \pm 2.42	99.32 \pm 1.52
3	99.58 \pm 0.16	98.90 \pm 0.13	98.67 \pm 2.32	97.80 \pm 1.95	99.43 \pm 1.71	91.02 \pm 2.54	99.95 \pm 0.15
4	91.77 \pm 4.46	100.00 \pm 0.00	87.97 \pm 8.52	76.94 \pm 12.44	94.96 \pm 6.94	77.69 \pm 7.11	99.06 \pm 1.15
5	98.01 \pm 2.22	100.00 \pm 0.00	82.52 \pm 12.16	91.32 \pm 4.90	99.80 \pm 0.30	92.58 \pm 1.70	96.10 \pm 2.82
6	99.43 \pm 0.63	100.00 \pm 0.00	96.13 \pm 4.72	98.17 \pm 4.30	100.00 \pm 0.00	86.53 \pm 3.49	100.00 \pm 0.00
7	100.00 \pm 0.00	100.00 \pm 0.00	99.07 \pm 1.69	96.63 \pm 10.11	99.58 \pm 1.26	97.85 \pm 1.14	100.00 \pm 0.00
8	90.67 \pm 3.15	94.61 \pm 0.42	92.19 \pm 2.97	95.80 \pm 3.23	98.24 \pm 2.13	83.66 \pm 2.78	99.54 \pm 0.77
9	98.20 \pm 2.02	83.53 \pm 6.20	1.11 \pm 2.15	98.45 \pm 4.33	98.47 \pm 4.33	96.96 \pm 1.24	99.76 \pm 0.48
10	100.00 \pm 0.00	100.00 \pm 0.00	99.28 \pm 1.32	97.66 \pm 1.53	100.00 \pm 0.00	96.40 \pm 3.17	100.00 \pm 0.00
11	99.77 \pm 0.34	100.00 \pm 0.00	99.46 \pm 0.61	98.80 \pm 1.77	98.51 \pm 2.03	99.88 \pm 0.25	99.93 \pm 0.20
12	99.05 \pm 1.75	87.67 \pm 0.18	95.41 \pm 5.15	95.84 \pm 1.77	99.84 \pm 0.32	97.83 \pm 1.48	100.00 \pm 0.00
13	100.00 \pm 0.00	100.00 \pm 0.00	99.84 \pm 0.47	100.00 \pm 0.00	100.00 \pm 0.00	100.00 \pm 0.00	100.00 \pm 0.00
OA (%)	98.04 \pm 0.59	94.70 \pm 1.08	96.46 \pm 1.02	96.80 \pm 0.98	99.22 \pm 0.58	93.81 \pm 1.05	99.71 \pm 0.17
AA (%)	97.92 \pm 0.59	95.12 \pm 0.64	94.61 \pm 1.45	95.59 \pm 0.99	99.10 \pm 0.71	92.96 \pm 0.87	99.48 \pm 0.30
$\kappa \times 100$	97.81 \pm 0.66	94.11 \pm 1.19	96.04 \pm 1.14	96.43 \pm 1.09	99.13 \pm 0.64	93.11 \pm 1.16	99.68 \pm 0.19

results further underscore the robustness and superiority of the proposed method.

D. Parameter Analysis

Comprehensive sensitivity experiments are conducted to assess three critical hyperparameters: the historical prediction queue's window size, the dynamic historical fusion weight α , and the number of training samples.

Historical window size: Three schemes are designed: fixed window (100) and dynamically increasing windows (50–300, 100–300, and 100–400). The fixed window evaluates

the impact of a constant historical length on pseudo-label stability, whereas the dynamic window accommodates varying requirements across training stages—starting with shorter windows initially and gradually expanding to incorporate more historical information. Experimental results show that the dynamic window scheme with range 50–300 achieves optimal performance, indicating that moderate window growth establishes a favorable balance between convergence speed and stability. In comparison, schemes with fixed window or excessive/insufficient growth rate exhibit relatively inferior performance, as shown in Fig 6.

TABLE V
CLASSIFICATION RESULTS FOR THE BOTSWANA DATASET WITH 10 LABELED SAMPLES PER CLASS.

No.	A2S2K	DMSGer	SSTN	CTF-SSCL	DEMAE	RMAE	Ours
1	99.04 \pm 1.56	96.65 \pm 2.86	99.21 \pm 0.51	99.96 \pm 0.12	99.31 \pm 1.60	100.00 \pm 0.05	98.54 \pm 1.59
2	100.00 \pm 0.00	100.00 \pm 0.00	100.00 \pm 0.00	99.56 \pm 1.01	100.00 \pm 0.00	100.00 \pm 0.00	100.00 \pm 0.00
3	100.00 \pm 0.00	98.80 \pm 0.46	100.00 \pm 0.00	99.54 \pm 0.51	94.85 \pm 10.29	99.17 \pm 1.26	99.84 \pm 0.29
4	100.00 \pm 0.00	100.00 \pm 0.00	100.00 \pm 0.00	99.56 \pm 0.88	100.00 \pm 0.00	100.00 \pm 0.00	100.00 \pm 0.00
5	91.73 \pm 1.30	93.90 \pm 0.24	99.16 \pm 0.65	90.93 \pm 4.81	96.06 \pm 2.87	98.30 \pm 2.02	95.18 \pm 3.92
6	82.41 \pm 9.82	93.86 \pm 0.31	96.82 \pm 0.86	98.11 \pm 1.56	98.07 \pm 2.25	94.90 \pm 1.02	99.81 \pm 0.42
7	100.00 \pm 0.00	99.92 \pm 0.07	100.00 \pm 0.00	98.84 \pm 2.98	100.00 \pm 0.00	100.00 \pm 0.00	99.64 \pm 0.77
8	99.23 \pm 0.95	99.90 \pm 0.37	100.00 \pm 0.00	94.87 \pm 10.28	98.55 \pm 4.02	100.00 \pm 0.00	99.58 \pm 0.78
9	91.77 \pm 6.24	99.97 \pm 0.60	99.93 \pm 0.21	97.14 \pm 4.08	99.01 \pm 2.96	95.99 \pm 3.18	99.97 \pm 0.10
10	100.00 \pm 0.00	100.00 \pm 0.00	100.00 \pm 0.00	99.16 \pm 1.50	100.00 \pm 0.00	100.00 \pm 0.00	100.00 \pm 0.00
11	99.54 \pm 0.57	100.00 \pm 0.00	100.00 \pm 0.00	99.46 \pm 0.71	100.00 \pm 0.00	100.00 \pm 0.00	99.49 \pm 1.18
12	99.94 \pm 0.19	79.83 \pm 6.99	100.00 \pm 0.00	99.88 \pm 0.35	99.88 \pm 0.23	99.53 \pm 0.68	100.00 \pm 0.00
13	99.44 \pm 0.81	100.00 \pm 0.00	99.71 \pm 0.50	99.57 \pm 0.91	98.37 \pm 4.28	98.53 \pm 0.62	100.00 \pm 0.00
14	99.33 \pm 1.23	100.00 \pm 0.00	83.54 \pm 5.42	99.41 \pm 0.79	100.00 \pm 0.00	100.00 \pm 0.00	98.12 \pm 5.95
OA (%)	96.78 \pm 0.89	96.67 \pm 0.42	99.11 \pm 0.14	98.14 \pm 0.83	98.73 \pm 1.57	98.83 \pm 0.35	99.19 \pm 0.40
AA (%)	97.32 \pm 0.74	97.33 \pm 0.36	98.45 \pm 0.38	98.29 \pm 0.82	98.87 \pm 1.42	99.03 \pm 0.29	99.22 \pm 0.49
$\kappa \times 100$	96.50 \pm 0.96	96.39 \pm 0.46	99.03 \pm 0.15	97.98 \pm 0.90	98.62 \pm 1.70	98.73 \pm 0.38	99.12 \pm 0.44

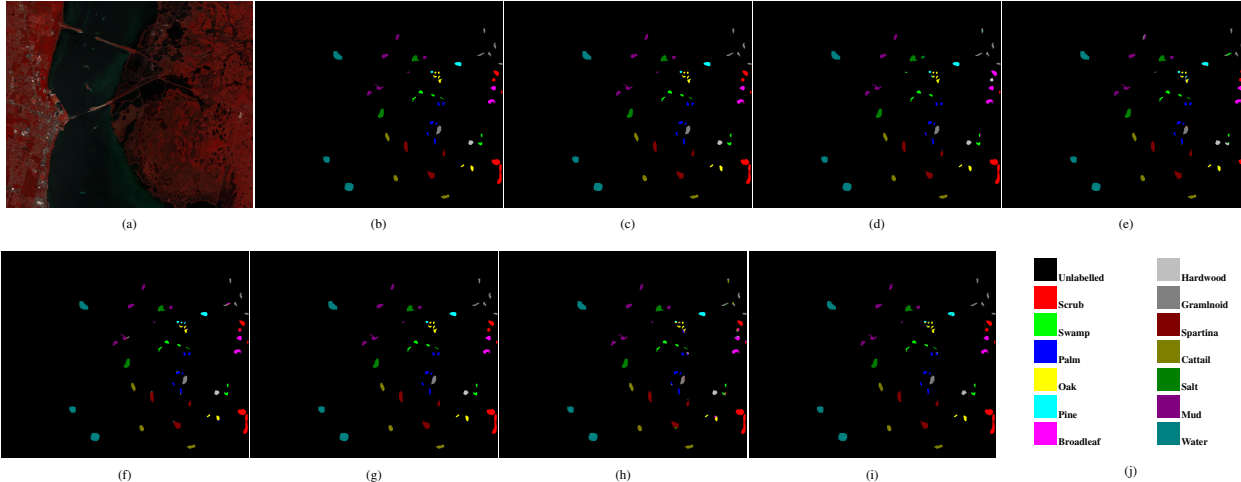


Fig. 4. Classification maps for the KSC dataset. (a) False color image. (b) Ground-truth. (c) A2S2K. (d) DMSGer. (e) SSTN. (f) CTF-SSCL. (g) DEMAЕ. (h) RMAE. (i) Ours. (j) Color labels

TABLE VI
ABLATION STUDY OF KEY MODULES ON FOUR REPRESENTATIVE DATASETS.

Dataset	Metrics	w/o EASLP	w/o DHP	w/o ATSC	Ours
PaviaU	OA (%)	92.66 \pm 2.53	94.20 \pm 1.50	94.87 \pm 1.32	95.21 \pm 1.17
	AA (%)	91.45 \pm 1.90	94.22 \pm 0.80	93.97 \pm 1.35	94.46 \pm 1.48
	$\kappa \times 100$	90.09 \pm 3.13	92.37 \pm 1.92	93.21 \pm 1.75	93.67 \pm 1.54
Houston2013	OA (%)	88.90 \pm 1.33	89.38 \pm 1.64	89.16 \pm 1.39	89.77 \pm 1.17
	AA (%)	90.17 \pm 0.86	90.56 \pm 1.31	90.35 \pm 1.18	90.87 \pm 0.98
	$\kappa \times 100$	88.00 \pm 1.44	88.52 \pm 1.78	88.28 \pm 1.51	88.94 \pm 1.26
KSC	OA (%)	99.60 \pm 0.13	99.66 \pm 0.14	99.65 \pm 0.14	99.71 \pm 0.17
	AA (%)	99.43 \pm 0.82	99.44 \pm 0.22	99.40 \pm 0.25	99.48 \pm 0.30
	$\kappa \times 100$	99.58 \pm 0.17	99.62 \pm 0.16	99.60 \pm 0.16	99.68 \pm 0.19
Botswana	OA (%)	99.18 \pm 0.53	99.18 \pm 0.53	99.12 \pm 0.46	99.19 \pm 0.40
	AA (%)	99.20 \pm 0.54	99.20 \pm 0.54	99.09 \pm 0.39	99.22 \pm 0.49
	$\kappa \times 100$	99.11 \pm 0.57	99.11 \pm 0.57	99.03 \pm 0.36	99.12 \pm 0.44

Dynamic historical fusion weight α : Five ranges are designed: 0.1–0.2, 0.1–0.3, 0.1–0.4, 0.1–0.5, and 0.1–0.6.

Results demonstrate that the model achieves optimal performance across all four datasets when the upper bound is set to 0.4. On PaviaU, performance peaks at 95.21% OA, 94.46% AA, and 93.67% Kappa, respectively. Expanding the upper bound to 0.5 or 0.6 causes performance deterioration, with Houston2013 showing significant OA/Kappa declines. This reveals that excessive α values render pseudo-label updates too conservative, resulting in compromised adaptability to new patterns. The 0.1–0.4 range is consequently identified as the optimal balance for effective operation (Fig 7).

The number of training samples: A comprehensive scaling analysis is performed using 5–25 labeled samples per class at 5-sample intervals. The results indicates a monotonic improvement in OA and AA with increasing sample size. The proposed method sustains superior performance across all data regimes, confirming its robustness in few-shot scenarios.

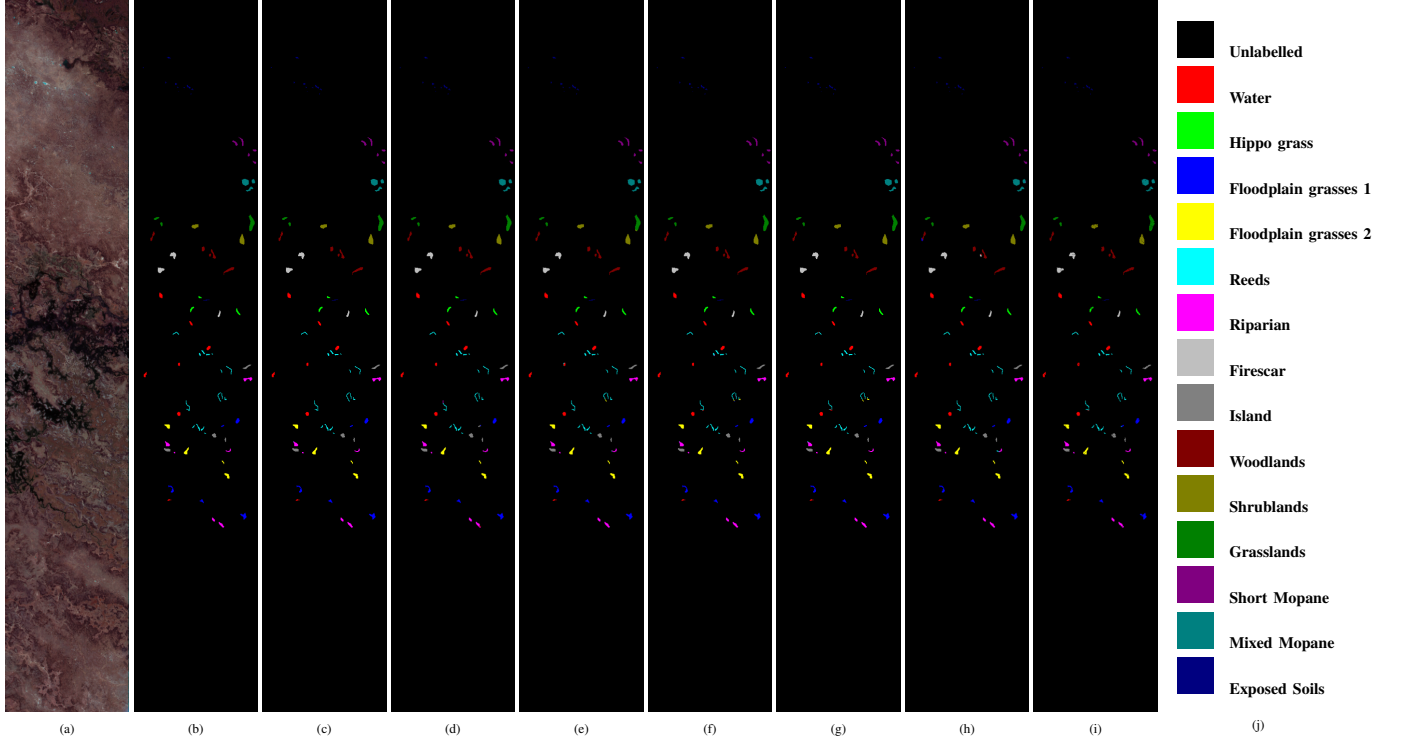


Fig. 5. Classification maps for the Botswana dataset. (a) False color image. (b) Ground-truth. (c) A2S2K. (d) DMSGer. (e) SSTN. (f) CTF-SSCL. (g) DEMAЕ. (h) RMAE. (i) Ours. (j) Color labels

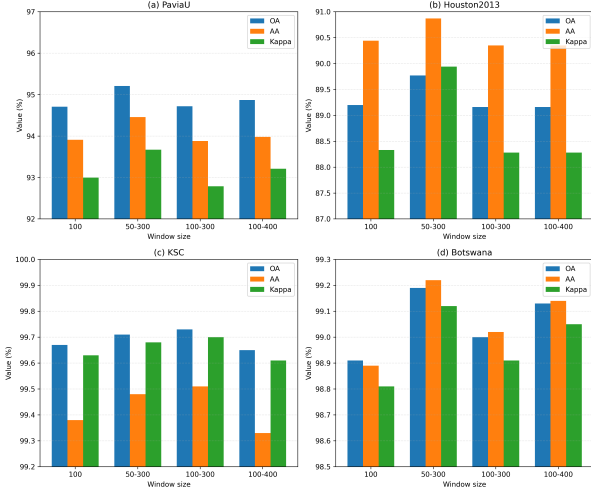


Fig. 6. Sensitivity analysis on the historical window size across different datasets.

E. Ablation Experiments

Three ablation experiments are designed to validate the module effectiveness. As shown in Table VI, results across four datasets demonstrate component contributions, with peak performances marked in bold.

EASLP: Removing the EASLP module (w/o EASLP) causes noticeable performance degradation across all datasets. The most pronounced drop occurs on PaviaU (OA: 95.21% \rightarrow 92.66%), followed by 1–2% decreases on Houston2013 and variable declines on KSC/Botswana. This consistent degradation confirms the critical role of spatial structural con-

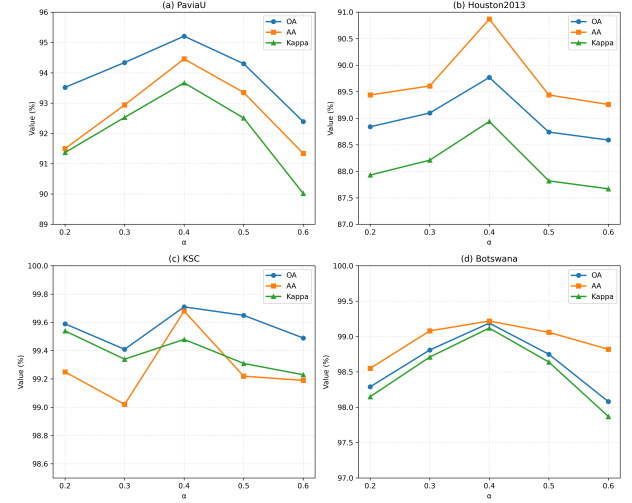


Fig. 7. Sensitivity analysis on the dynamic historical fusion weight α across different datasets.

straints, revealing the insufficiency of spectral features alone.

DHP: Ablating the DHP module (w/o DHP) causes marginal but consistent degradation in OA/AA/Kappa. While its quantitative improvement is less dramatic than other components, it fundamentally improves training stability by leveraging historical information to suppress pseudo-label fluctuations and ensure smoother convergence. Although the performance improvement brought by this module is less pronounced than that of the previous two modules, it significantly enhanced the robustness of training. With the incorporation of historical information, the temporal fluctuation of pseudo-

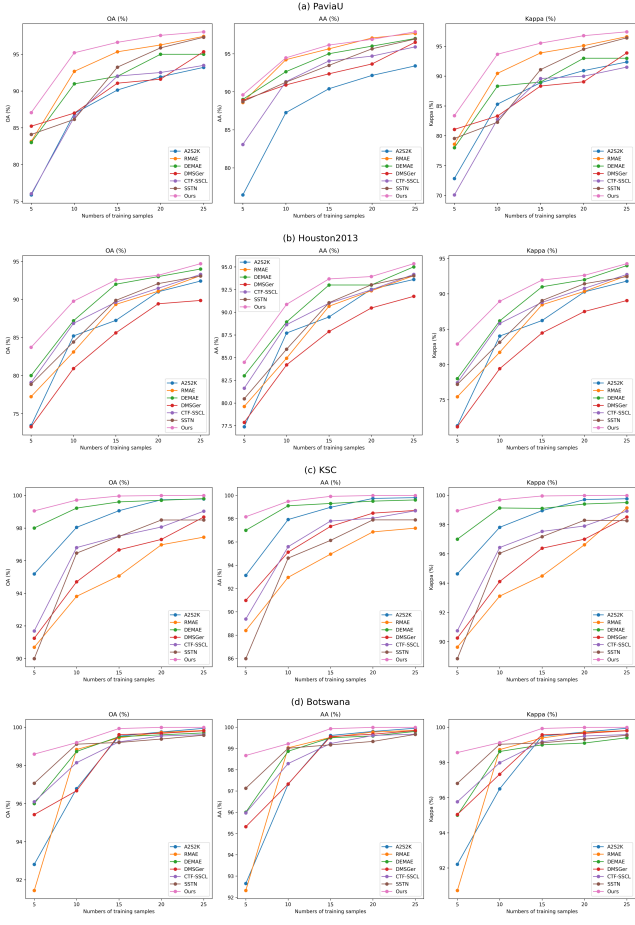


Fig. 8. Overall accuracies with respect to different numbers of training samples on four datasets.

labels is reduced, leading to more stable model convergence. This capability proves especially valuable in few-shot or high-noise scenarios by effectively mitigating error accumulation.

ATSC: We remove the ATSC module (w/o ATSC), relying solely on confidence scores from fused historical and current predictions. A fixed threshold of 0.95 is applied for binary categorization of all unlabeled samples. Results show quantifiable performance deterioration across all four datasets—approximately 1% OA/AA drops on PaviaU and Houston2013, with KSC/Botswana showing smaller declines but increased standard deviation, indicating pseudo-label instability. The Count-Gap mechanism proves essential for consistency-based sample stratification and robust pseudo-labeling.

IV. CONCLUSION

The proposed semi-supervised framework for hyperspectral image classification seamlessly integrates spatial prior information with dynamic learning mechanism, achieving substantial gains in feature extraction and classification performance. Confronting the dual challenges of high annotation costs and limited sample availability, the incorporated EASLP module successfully alleviates label diffusion originating from superpixel segmentation, consequently strengthening classification robustness in boundary regions. Furthermore, the DHP

method enhances temporal consistency and noise robustness by smoothing pseudo-label fluctuations. The ATSC strategy improves pseudo-label quality and learning efficiency through hierarchical sample utilization. By synergistically integrating DHP and ATSC, the proposed DREPL framework achieves spatiotemporal synchronization, thereby boosting classification performance.

Results validate the efficacy of our framework in few-shot HSI classification with robust performance. However, the proposed method is inherently constrained by single-scene applicability and unaddressed domain adaptation needs. Subsequent investigations should prioritize cross-domain generalization and transferability enhancements for multi-scene applications.

ACKNOWLEDGMENT

This work was supported by the Basic Scientific Research Project of the Education Department of Liaoning Province (Key Project of Independent Topic Selection, 2024), Grant No. 524053218.

REFERENCES

- [1] S. Zhang, X. Kang, P. Duan, B. Sun, and S. Li, “Polygon structure-guided hyperspectral image classification with single sample for strong geometric characteristics scenes,” *IEEE Trans. Geosci. Remote Sens.*, vol. 60, pp. 1–12, 2022, doi: 10.1109/TGRS.2021.3094582.
- [2] G. Sun, Z. Jiao, A. Zhang, F. Li, H. Fu, and Z. Li, “Hyperspectral image-based vegetation index (HSV): A new vegetation index for urban ecological research,” *Int. J. Appl. Earth Observ. Geoinf.*, vol. 103, p. 102529, 2021, doi: 10.1016/j.jag.2021.102529.
- [3] Q. Du, “Unsupervised real-time constrained linear discriminant analysis to hyperspectral image classification,” *Pattern Recognit.*, vol. 40, no. 5, pp. 1510–1519, 2007, doi: 10.1016/j.patcog.2006.08.006.
- [4] N. Yokoya, J. C.-W. Chan, and K. Segl, “Potential of resolution-enhanced hyperspectral data for mineral mapping using simulated EnMAP and Sentinel-2 images,” *Remote Sens.*, vol. 8, p. 172, 2016, doi: 10.3390/rs8030172.
- [5] M. Shimoni, R. Haelterman, and C. Perneel, “Hyperspectral imaging for military and security applications: Combining myriad processing and sensing techniques,” *IEEE Geosci. Remote Sens. Mag.*, vol. 7, no. 2, pp. 101–117, 2019, doi: 10.1109/MGRS.2019.2902525.
- [6] P. Ghamisi *et al.*, “New frontiers in spectral-spatial hyperspectral image classification: The latest advances based on mathematical morphology, Markov random fields, segmentation, sparse representation, and deep learning,” *IEEE Geosci. Remote Sens. Mag.*, vol. 6, no. 3, pp. 10–43, 2018, doi: 10.1109/MGRS.2018.2854840.
- [7] S. Li, W. Song, L. Fang, Y. Chen, P. Ghamisi, and J. A. Benediktsson, “Deep learning for hyperspectral image classification: An overview,” *IEEE Trans. Geosci. Remote Sens.*, vol. 57, no. 9, pp. 6690–6709, 2019, doi: 10.1109/TGRS.2019.2907932.
- [8] S. Jia, S. Jiang, Z. Lin, N. Li, M. Xu, and S. Yu, “A survey: Deep learning for hyperspectral image classification with few labeled samples,” *Neurocomputing*, vol. 448, pp. 179–204, 2021, doi: 10.1016/j.neucom.2021.03.035.
- [9] P. Polewski, W. Yao, M. Heurich, P. Krzystek, and U. Stilla, “Combining active and semisupervised learning of remote sensing data within a Rényi entropy regularization framework,” *IEEE J. Sel. Topics Appl. Earth Observ. Remote Sens.*, vol. 9, no. 7, pp. 2910–2922, 2016.
- [10] P. Wang and W. Yao, “A new weakly supervised approach for ALS point cloud semantic segmentation,” *ISPRS J. Photogramm. Remote Sens.*, vol. 188, pp. 237–254, 2022.
- [11] C. Zhao, W. Zhu, and S. Feng, “Superpixel guided deformable convolution network for hyperspectral image classification,” *IEEE Trans. Image Process.*, vol. 31, pp. 3838–3851, 2022.
- [12] C. Shi, Z. Lv, H. Shen, L. Fang, and Z. You, “Improved metric learning with the CNN for very-high-resolution remote sensing image classification,” *IEEE J. Sel. Topics Appl. Earth Obs. Remote Sens.*, vol. 14, pp. 631–644, 2020.

- [13] C. Shi, L. Fang, Z. Lv, and M. Zhao, "Explainable scale distillation for hyperspectral image classification," *Pattern Recognit.*, vol. 122, p. 108316, 2022.
- [14] Y. Dong, Q. Liu, B. Du, and L. Zhang, "Weighted feature fusion of convolutional neural network and graph attention network for hyperspectral image classification," *IEEE Trans. Image Process.*, vol. 31, pp. 1559–1572, 2022.
- [15] H. Lee and H. Kwon, "Going deeper with contextual CNN for hyperspectral image classification," *IEEE Trans. Image Process.*, vol. 26, no. 10, pp. 4843–4855, 2017, doi: 10.1109/TIP.2017.2725580.
- [16] Z. Zhong, J. Li, Z. Luo, and M. Chapman, "Spectral–spatial residual network for hyperspectral image classification: A 3-D deep learning framework," *IEEE Trans. Geosci. Remote Sens.*, vol. 56, no. 2, pp. 847–858, 2018, doi: 10.1109/TGRS.2017.2755542.
- [17] S. K. Roy, G. Krishnan, S. R. Dubey, and B. B. Chaudhuri, "HybridSN: Exploring 3-D–2-D CNN feature hierarchy for hyperspectral image classification," *IEEE Geosci. Remote Sens. Lett.*, vol. 17, no. 2, pp. 277–281, 2020, doi: 10.1109/LGRS.2019.2918719.
- [18] S. K. Roy, S. Manna, T. Song, and L. Bruzzone, "Attention-based adaptive spectral–spatial kernel ResNet for hyperspectral image classification," *IEEE Trans. Geosci. Remote Sens.*, vol. 59, no. 9, pp. 7831–7843, 2021, doi: 10.1109/TGRS.2020.3043267.
- [19] Z. Zhong, Y. Li, L. Ma, J. Li, and W.-S. Zheng, "Spectral–spatial transformer network for hyperspectral image classification: A factorized architecture search framework," *IEEE Trans. Geosci. Remote Sens.*, vol. 60, pp. 1–15, 2022, doi: 10.1109/TGRS.2021.3115699.
- [20] L. Fang, X. Lan, T. Li, and H. Shen, "PCET: Patch confidence-enhanced transformer with efficient spectral–spatial features for hyperspectral image classification," *Int. J. Appl. Earth Observ. Geoinf.*, vol. 136, p. 104308, 2025, doi: 10.1016/j.jag.2024.104308.
- [21] K. Gao, B. Liu, X. Yu, and A. Yu, "Unsupervised meta learning with multiview constraints for hyperspectral image small sample set classification," *IEEE Trans. Image Process.*, vol. 31, pp. 3449–3462, 2022, doi: 10.1109/TIP.2022.3169689.
- [22] P. Vincent, H. Larochelle, Y. Bengio, and P.-A. Manzagol, "Extracting and composing robust features with denoising autoencoders," in *Proc. Int. Conf. Mach. Learn. (ICML)*, 2008, pp. 1096–1103, doi: 10.1145/1390156.1390294.
- [23] C. Tao, H. Pan, Y. Li, and Z. Zou, "Unsupervised spectral–spatial feature learning with stacked sparse autoencoder for hyperspectral imagery classification," *IEEE Geosci. Remote Sens. Lett.*, vol. 12, no. 12, pp. 2438–2442, 2015, doi: 10.1109/LGRS.2015.2482520.
- [24] Y. Tarabalka, J. Á. Benediktsson, and J. Chanussot, "Spectral–spatial classification of hyperspectral imagery based on partitional clustering techniques," *IEEE Trans. Geosci. Remote Sens.*, vol. 47, no. 8, pp. 2973–2987, 2009, doi: 10.1109/TGRS.2009.2016214.
- [25] P. Lu, X. Jiang, Y. Zhang, X. Liu, Z. Cai, J. Jiang, and A. Plaza, "Spectral–spatial and superpixelwise unsupervised linear discriminant analysis for feature extraction and classification of hyperspectral images," *IEEE Trans. Geosci. Remote Sens.*, vol. 61, pp. 1–15, 2023, doi: 10.1109/TGRS.2023.3330474.
- [26] Y. He, W. Liang, D. Zhao, H.-Y. Zhou, W. Ge, Y. Yu, and W. Zhang, "Attribute surrogates learning and spectral tokens pooling in transformers for few-shot learning," *Proc. IEEE/CVF Conf. Comput. Vis. Pattern Recognit. (CVPR)*, 2022, pp. 9119–9129.
- [27] H. Liu, Z. Ye, W.-S. Hu, Z. Cao, and W. Li, "Spatial–spectral hierarchical multiscale transformer-based masked autoencoder for hyperspectral image classification," *IEEE J. Sel. Topics Appl. Earth Observ. Remote Sens.*, vol. 18, pp. 12150–12165, 2025, doi: 10.1109/JSTARS.2025.3565562.
- [28] M. Liang, W. Wu, H. Shen, L. Yu, X. Yu, and L. Jiao, "SuperCoT-X: Masked hyperspectral image modeling with diverse superpixel-level contrastive tokenizer," *IEEE J. Sel. Topics Appl. Earth Obs. Remote Sens.*, 2025.
- [29] Z. Li, Z. Xue, M. Jia, X. Nie, H. Wu, M. Zhang, and H. Su, "DEMAE: Diffusion-enhanced masked autoencoder for hyperspectral image classification with few labeled samples," *IEEE Trans. Geosci. Remote Sens.*, vol. 62, pp. 1–16, 2024, doi: 10.1109/TGRS.2024.3445991.
- [30] L. Wang, H. Wang, P. Wang, and L. Wang, "Regularized masked auto-encoder for semi-supervised hyperspectral image classification," *IEEE Trans. Geosci. Remote Sens.*, vol. 62, pp. 1–21, 2024, doi: 10.1109/TGRS.2024.3509720.
- [31] R. Huang, Y. Xu, D. Hong, W. Yao, P. Ghamisi, and U. Stilla, "Deep point embedding for urban classification using ALS point clouds: A new perspective from local to global," *ISPRS J. Photogramm. Remote Sens.*, vol. 163, pp. 62–81, 2020.
- [32] I. Nassar, M. Hayat, E. Abbasnejad, H. Rezatofighi, and G. Hafari, "ProtoCon: Pseudo-label refinement via online clustering and prototypical consistency for efficient semi-supervised learning," in *Proc. IEEE/CVF Conf. Comput. Vis. Pattern Recognit. (CVPR)*, 2023, pp. 11641–11650.
- [33] T. Chen, S. Lu, and J. Fan, "SS-HCNN: Semi-supervised hierarchical convolutional neural network for image classification," *IEEE Trans. Image Process.*, vol. 28, no. 5, pp. 2389–2398, 2019.
- [34] Y. Oh, D.-J. Kim, and I. S. Kweon, "DASO: Distribution-aware semantics-oriented pseudo-label for imbalanced semi-supervised learning," in *Proc. IEEE/CVF Conf. Comput. Vis. Pattern Recognit. (CVPR)*, 2022, pp. 9786–9796.
- [35] M. Li, Q. Li, and Y. Wang, "Class-balanced adaptive pseudo labeling for federated semi-supervised learning," in *Proc. IEEE/CVF Conf. Comput. Vis. Pattern Recognit. (CVPR)*, 2023, pp. 16292–16301.
- [36] H. Wu and S. Prasad, "Semi-supervised deep learning using pseudo labels for hyperspectral image classification," *IEEE Trans. Image Process.*, vol. 27, no. 3, pp. 1259–1270, 2018, doi: 10.1109/TIP.2017.2772836.
- [37] X. Zhu, Z. Ghahramani, and J. D. Lafferty, "Semi-supervised learning using Gaussian fields and harmonic functions," in *Proc. Int. Conf. Mach. Learn. (ICML)*, 2003, pp. 912–919.
- [38] J. Li, C. Xiong, and S. C. H. Hoi, "CoMatch: Semi-supervised learning with contrastive graph regularization," in *Proc. IEEE/CVF Int. Conf. Comput. Vis. (ICCV)*, 2021, pp. 9194–9203, doi: 10.1109/ICCV48922.2021.00934.
- [39] Y. Ouali, C. Hudelot, and M. Tami, "Semi-supervised semantic segmentation with cross-consistency training," in *Proc. IEEE/CVF Conf. Comput. Vis. Pattern Recognit. (CVPR)*, 2020, pp. 12671–12681, doi: 10.1109/CVPR42600.2020.01269.
- [40] A. Tarvainen and H. Valpola, "Mean teachers are better role models: Weight-averaged consistency targets improve semi-supervised deep learning results," in *Adv. Neural Inf. Process. Syst.*, 2017, pp. 1195–1204.
- [41] Y. Yang, X. Tang, X. Zhang, J. Ma, F. Liu, and X. Jia, "Semi-supervised multiscale dynamic graph convolution network for hyperspectral image classification," *IEEE Trans. Neural Netw. Learn. Syst.*, vol. 35, no. 5, pp. 6806–6820, 2024, doi: 10.1109/TNNLS.2022.3212985.
- [42] B. Xi, Y. Zhang, J. Li, Y. Li, Z. Li, and J. Chanussot, "CTF-SSCL: CNN-transformer for few-shot hyperspectral image classification assisted by semisupervised contrastive learning," *IEEE Trans. Geosci. Remote Sens.*, vol. 62, pp. 1–17, 2024, doi: 10.1109/TGRS.2024.3465225.
- [43] Z. Li, Y. Wang, L. Wang, F. Guo, Y. Yang, and J. Wei, "Pseudolabeling contrastive learning for semisupervised hyperspectral and LiDAR data classification," *IEEE J. Sel. Top. Appl. Earth Obs. Remote Sens.*, vol. 17, pp. 17099–17116, 2024, doi: 10.1109/JSTARS.2024.3452494.
- [44] L. Liu, H. Zhang, and Y. Wang, "Contrastive mutual learning with pseudo-label smoothing for hyperspectral image classification," *IEEE Trans. Instrum. Meas.*, vol. 73, pp. 1–14, 2024, doi: 10.1109/TIM.2024.3406811.
- [45] E. Arazo, D. Ortego, P. Albert, N. E. O'Connor, and K. McGuinness, "Pseudo-labeling and confirmation bias in deep semi-supervised learning," in *Proc. Int. Joint Conf. Neural Netw. (IJCNN)*, 2020, pp. 1–8, doi: 10.1109/IJCNN48605.2020.9207304.
- [46] K. Sohn, D. Berthelot, C.-L. Li, Z. Zhang, N. Carlini, E. D. Cubuk, A. Kurakin, H. Zhang, and C. Raffel, "FixMatch: Simplifying semi-supervised learning with consistency and confidence," in *Adv. Neural Inf. Process. Syst. (NeurIPS)*, 2020.
- [47] Q. Xie, Z. Dai, E. Hovy, T. Luong, and Q. V. Le, "Unsupervised data augmentation for consistency training," in *Adv. Neural Inf. Process. Syst. (NeurIPS)*, vol. 33, pp. 6256–6268, 2020.
- [48] R. Achanta, A. Shaji, K. Smith, A. Lucchi, P. Fua, and S. Süsstrunk, "SLIC superpixels compared to state-of-the-art superpixel methods," *IEEE Trans. Pattern Anal. Mach. Intell.*, vol. 34, no. 11, pp. 2274–2282, 2012, doi: 10.1109/TPAMI.2012.120.